Journal of Microscopy, Vol. 233, Pt 3 2009, pp. 404–416
Received 18 February 2008; accepted 23 October 2008

Isotropic high-resolution three-dimensional confocal micro-rotation imaging for non-adherent living cells

B. LE SAUX*, B. CHALMOND*, Y. YU*, A. TROUVÉ*,
O. RENAUD† & S.L. SHORTE†
* *CMLA, Ecole Normale Supérieure de Cachan, CNRS, UniverSud 61 Avenue Président Wilson, 94230 Cachan, Cedex, France*
†*Plateforme d'Imagerie Dynamique (PFID), Imagopole Institut Pasteur, 25-28 rue du Dr. Roux, Paris 75015, France*

Key words. Deconvolution, EM algorithm, incomplete coverage, interpolation, isotropic high resolution, micro-rotation confocal microscopy, non-organized data, reconstruction from projection, PSF with spatial-varying orientation, z-stack.

Summary

Recently, micro-rotation confocal microscopy has enabled the acquisition of a sequence of micro-rotated images of nonadherent living cells obtained during a partially controlled rotation movement of the cell through the focal plane. Although we are now able to estimate the three-dimensional position of every optical section with respect to the cell frame, the reconstruction of the cell from the positioned micro-rotated images remains a last task that this paper addresses. This is not strictly an interpolation problem since a micro-rotated image is a convoluted two-dimensional map of a three-dimensional reality. It is rather a 'reconstruction from projection' problem where the term projection is associated to the PSF of the deconvolution process. Micro-rotation microscopy has a specific difficulty. It does not yield a complete coverage of the volume. In this paper, experiments illustrate the ability of the classical EM algorithm to deconvolve efficiently cell volume despite of the incomplete coverage. This cell reconstruction method is compared to a kernel-based method of interpolation, which does not take account explicitly the point-spread-function (PSF). It is also compared to the standard volume obtained from a conventional z-stack. Our results suggest that deconvolution of micro-rotation image series opens some exciting new avenues for further analysis, ultimately laying the way towards establishing an enhanced resolution 3D light microscopy.

Introduction

Our microscope is equipped with a dielectrophoretic field control microelectrode cage that enables trapping of nonadherent living cells (Schnelle *et al.*, 1993; Lizundia *et al.*, 2005; Renaud *et al.*, 2008). Once a cell has been trapped, it undergoes continuous unstable rotations around a main axis (Shorte *et al.*, 2003). During the rotation, a sequence of microscopic images $(S^k)_{1\leq k\leq N}$ is obtained through the fixed focal plane F at a given rate. Each image is taken under the same microscopic conditions. Figure 6 (first column) shows three images extracted from a sequence of 280 micro-rotated images per turn of a cell in rotation. Among the advantages of such an apparatus, is the ability to alleviate the problem of anisotropy of the microscope resolution: the resolution perpendicular to the focal plane is two to three times lower than the resolution within the focal plane. That is translated into the point-spread-function (PSF) of the microscope, which is mainly elongated along the z-axis (see Fig. 5).

Since the images are all recorded in the fixed plane F, their positions inside the cell are unknown. However, these positions can be estimated using the method presented in Yu *et al.* (2007). So, here, we assume that the images have been aligned according to these positions. The situation where the cell is rotating and F is fixed is equivalent to the *dual* situation where the cell is fixed and F is rotating (see Fig. 3). Throughout these lines, we adopt the dual case. With this viewpoint, we understand that the PSF whose main axis is perpendicular to the focal plane has a spatially varying orientation with respect to the volume: each image has its own oriented PSF but the PSF shape remains the same during the cell revolution. Let us note that volume reconstruction from micro-rotated images is formally analogous to tomographic reconstruction from projections: in tomography, one point of the projection is modelled by the integral of the object over a straight line through the volume whereas in our case, one point in the image is modelled by a weighted integral of the

Correspondence to: Pr. B. Chalmond. Tel: (33) 1 47 40 59 00; fax: (33) 1 47 40 50 01; e-mail: Bernard.Chamond@cmla.ens-cachan.fr

object over the full volume, with weights given by the PSF of the microscope.

Another particularity arises from our microscope equipment. When F turns around an axis that is not included into it, a part of the 3D space is never intercepted by the moving plane, Fig. 3. Due to this incomplete coverage of the imaging volume, a 'black hole' is apparent in the 3D cell representation when this phenomena is not taken into account (see Fig. 7 (column 1), Fig. 8(b)). However, one image is not a perfect slice; it is a weighted integral over the full volume. Therefore, the voxels in the cell located in the 'black hole' contribute to the images (at least if the size of the hole is not too large with respect to the resolution of the microscope), and therefore the images may contain information about the voxels located in the black hole. This point explains why it is possible to reconstruct the cell in the area of the black hole.

In the *widefield* imaging domain, a first attempt of deconvolution of micro-rotated image series has been presented in Laksameethanasan *et al.* (2006) and extended in Laksameethanasan *et al.* (2008), using a classical approach as in our paper. Unfortunately, in this paper the authors ignore the black hole problem because they did not see it since they mainly perform experiments based on simulated data for which the rotation axis can be located within the focal plane. To be unaware of the black hole amounts to assume that the rotation axis lies in the focal plane. This property cannot be realized because today the dielectrophoretic field cage technology does not enable to control the cell movement with such an accuracy. The morphology of the cell and its interaction with the field implies an unstable movement that cannot guaranty the stability of the rotation axis.

The contribution of our paper is twofold: we present a deconvolution process taking into account the spatially varying orientation of the PSF and the incomplete coverage phenomena; and then we give a first evaluation of the reconstruction by comparison with two others 3D cell imaging. First, we experiment with the same protocol but using a simpler interpolation method that can only partly improve the resolution since the PSF is not used. It means that we directly interpolate a set of micro-rotated images of a convolved volume, and consequently, the resulting 3D volume is not a deconvolved volume, but rather a smooth representation of the reality. This first comparison helps to distinguish the pure interpolation effects from those arising from the deconvolution process. Second, an another protocol is considered: the conventional z-stack. Contrary to the micro-rotation protocol, the PSF orientation is here always oriented towards the z-direction independently of the image position. For this protocol, 3D cell imaging shows a poor resolution, but above all, it enables to see that the micro-rotation imaging is free from axial aberration.

Material and methods

The basic hardware consists of a 3D dielectrophoretic field cage comprising micro-electrodes fabricated photo lithographically on optically transparent glass substrates and assembled face-to-face (Fig. 1). Cells suspended in a buffered medium can be gently passed through the cage using an ultra-low-speed micro-fluidic control, and trapped then manipulated inside the cage using high-frequency polarization of dielectrics, creating forces in the range of pico-Newtons repelling particles from regions of high field strength towards electric field minima (Fig. 2). This principle permits approximately stable positioning of living cells within micrometer dimensions. The live cell-traping/rotator offers some degree of control over suspended cell (or other micro-object) position, and enables a rotational control. As the cell rotation progresses, snapshot images are recorded using a high-speed camera, and passing through 360° the cell is observed from multiple angles of view. This is far superior to existing 'through-stack' methods applied to adherent cells because it multiplies by at least a factor fold the available information content for subsequent processing.

Reconstruction method

Recall that we assume the cell is fixed and the focal plane is rotating. The focal plane is assimilated to a square grid, that is the image acquisition grid. In a given frame $\mathcal{R} = (oxyz)$, let m be the unknown cell volume defined on a square 3D grid G, such that the reference focal plane F is contained in (oxy). F^k denotes the position of the moving focal plane supporting the image S^k. When the focal plane is moving, the shape of the PSF

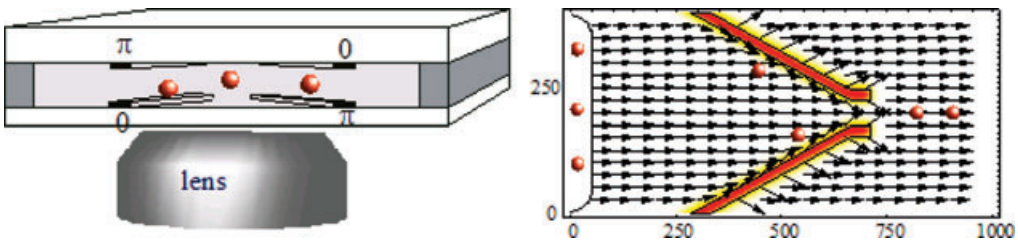

Fig. 1. Scheme of micro chamber for high-resolution optics. (a) Two electrode planes are mounted face-to-face to built a closed micro channel, (b) Electric field (red values correspond to high intensity) and combined particle guiding force distribution (arrows) in the central plane between the electrode planes.

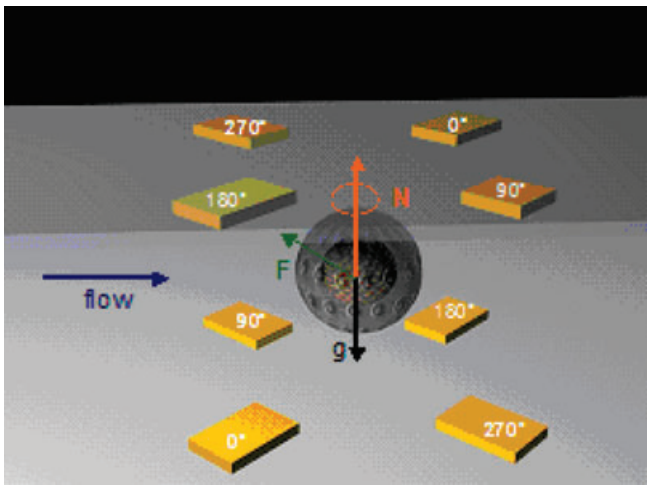

Fig. 2. Scheme of dielectrophoretic octode field cage with trapped cell.

Ψ_k remains unchanged but its orientation changes according to the movement of the focal plane since the main axis of the PSF is always perpendicular to F^k.

Interpolation without deconvolution

In this section, we limit our treatment to the interpolation task. It means that the PSF is not included into the image-formation model. It enables to experimentally analyze the effect of the deconvolution compared to the simple interpolation. Let us emphasize that this method is not an alternative method to the micro-rotation reconstruction by deconvolution. Practically, it enables to get quickly a 3D representation that allows to establish a first judgment on the reconstruction, as the absence of an axial aberration. In fact, an alternative method would be rather based on the fusion of several z-stacks as we shall analyze in a forthcoming paper.

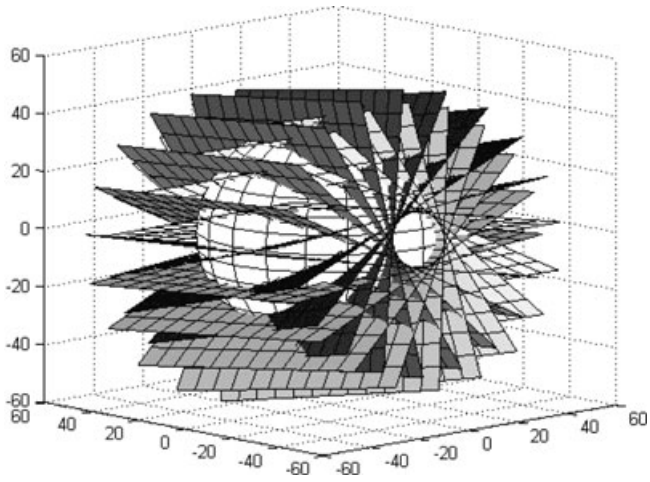

Fig. 3. Focal plane movement and black hole. In this example, the black hole is a cylinder and the rotation axis is confounded with the cylinder axis.

In the goal of interpolation and visualization, the nondeconvolved volume, says $\tilde{m}$, is defined as a continuous volume. We have to estimate $\tilde{m}$ given the sequence $\{S^k\}$. Using the well-known kernel-based modelling (Wahba, 1999), the continuous volume is written as a linear combination of functions $\mathcal{K}(g_r, \cdot)$, $g_r \in G$:

$$\tilde{m}(\cdot) = \sum_r \alpha_r \mathcal{K}(g_r, \cdot),$$

where $\mathcal{K}(\cdot, \cdot)$ is a kernel function modelling the spatial dependence within $\tilde{m}$:

$$\mathcal{K}(g, g') = \rho(||(g - g')||/\lambda_{\tilde{m}}), \quad \forall\, g, g' \in G\ .$$

With this definition, the volume $\tilde{m}$ is replaced by the unknown set of parameters (α_r). We have chosen the Gaussian function for ρ. $\lambda_{\tilde{m}}$ is a scale parameter that defines the range of the spatial dependence, as a covariance function does. Furthermore, it is well known that the norm of $\tilde{m}$ is

$$||\tilde{m}||^2_{\mathcal{H}} = \sum_{r,r'} \alpha_r \alpha_{r'}\, \mathcal{K}(g_r, g_{r'})\ .$$

We quantify the regularity of $\tilde{m}$ by its probability given by the Gaussian law:

$$P(\tilde{m}) \propto \exp\left(-\frac{\|\tilde{m}\|^2_{\mathcal{H}}}{2\sigma^2_{\tilde{m}}}\right), \tag{1}$$

where $\sigma^2_{\tilde{m}}$ is the regularization parameter that tunes the amplitude of the variations of $\tilde{m}$. Greater is the probability, and greater is the regularity of $\tilde{m}$ with respect to the kernel $\mathcal{K}$. On the other hand, every image S^k is a noisy version of the section $\tilde{m}(F^k)$: $S^k = \tilde{m}(F^k) + \epsilon$ where ϵ denotes a Gaussian white field:

$$P(S^k \,|\, \tilde{m}) \propto \exp\left(-\frac{\|S^k - \tilde{m}(F^k)\|^2}{2\sigma^2_\epsilon}\right)\ . \tag{2}$$

Following the Bayes rule, the estimate of α maximizes the posterior probability $P(\tilde{m} \mid \{S^k\}) \propto P(\tilde{m}) \prod_k P(S^k \mid \tilde{m})$, which is equivalent to maximize the following energy:

$$\mathcal{J}(\alpha) = \|\tilde{m}\|^2_{\mathcal{H}} + \frac{\sigma^2_{\tilde{m}}}{\sigma^2_\epsilon} \sum_{k=1}^{N} \|S^k - \tilde{m}(F^k)\|^2\ .$$

$\lambda_{\tilde{m}}$ and $\sigma^2_{\tilde{m}}$ are automatically estimated using the maximum likelihood principle (Yu *et al.*, 2007) given the observed sequence $\{S^k\}$. This is a key point because it is difficult to determine these parameters by sequential trials. This difficulty is amplified by the fact that the data are badly distributed: many data points are present around the rotation centre whereas far from this centre, data points are very sparse. So, it clear there is not only the black hole problem, but also a problem in the outer regions of the data where the slices fan out far. However, this fact is now less severe since our acquisition system is able to acquire near 300 hundred images per turn. Furthermore, note that the norm of regularization

$\|\tilde{m}\|_{\mathcal{H}}$ is not the common Tikhonov regularization norm that is not able, here, to deal with interpolation where the slices fan out far, since at these locations the interpolated values obtained with this norm tend to be abnormally small, (Yu *et al.*, 2008).

Reconstruction with deconvolution

Let m be the unknown volume not degraded by the PSF. Our goal is to estimate m given the sequence $\{S^k\}$. Computing 3D image convolution using a PSF with spatial-varying orientation is quite calculation-intensive. So, we use the following scheme that allows to use only the PSF Ψ associated to the reference focal plane F.

For every positioned focal plane F^k, let us define a 3D square grid G^k such that two faces are parallel to F^k and are at equal distance to F^k. G^k corresponds to the affine rotation that applies F to F^k. The node values of G^k are obtained by interpolation from those of G:

$$m_r^k = \sum_{j \in V_r^k} A_j^k m_j, \quad \forall r \in G_r^k,$$

where V_r^k is a neighbourhood of r in G. In matrix form, one write

$$m^k = A^k m\,. \tag{3}$$

Let H be the linear operator associated to the PSF Ψ. *With respect to the frame* G^k, we consider the model

$$\mathrm{E}[\mathbf{S}^k] = P\,H m^k, \tag{4}$$

where E denotes the mathematical expectation and $\mathbf{S}^k$ is the random vector whose S^k is an occurrence. P is the section operator $P : \mathbb{R}^{d^3} \longrightarrow \mathbb{R}^{d^2}$. Behind this formula is $\Psi_k \star m = \Psi \star m^k$. Finally, we get

$$\mathbf{E}[\mathbf{S}^k] = PHA^k m, \tag{5}$$

which models the relationship between the data and the unknown volume. Below, we will denote $\mathcal{H}^k \doteq PHA^k$.

Image deconvolution is an old problem for which a well-known solution is given by the original Lucy–Richardson algorithm (Richardson, 1972; Lucy, 1974). In this context, this algorithm can be formalized in the general framework of the EM algorithm (Dempster *et al.*, 1977; Shepp & Vardi, 1982). In our case, m is defined over the grid G, which is larger than the data support $\mathcal{F} = \{F^k\}$ all the more so the black hole is large. Although our data are nonuniformly distributed over G, they are well ordered through the image series. The application of the EM algorithm is computer-intensive. Its convergence can be accelerated by processing the data in ordered subsets corresponding to the micro-rotated images within each EM iteration (Hudson & Larkin, 1994).

Let us recall briefly the EM algorithm for deconvolution as introduced in Shepp & Vardi (1982) in order to rewrite it with the spatially- varying orientation of the PSF as defined above. For every site $i \in \mathcal{F}$ and $j \in G$, let x_{ij} be the number of photons received at i and coming from j. The observations are then given by $S_i^k = \sum_j x_{ij}$ and we assume that, given m_j, x_{ij} is the occurrence of a Poisson random variable $\mathcal{P}(\mathcal{H}_{ij}^k m_j)$. Under the hypothesis of independence of the x_{ij}, S_i^k is the occurrence of the Poisson random variable $\mathcal{P}(\sum_j \mathcal{H}_{ij}^k m_j)$.

From this model, we aim to find an estimate of m that maximizes the likelihood of $p(S|m)$. The general EM algorithm (Dempster *et al.*, 1977) works with the following expected log-likelihood

$$Q(m|m(t)) = \mathbf{E}\left[\log(p(X|m))|S, m(t)\right], \tag{6}$$

with respect to the conditional distribution $p(x|S, m(t))$ where $m(t)$ is a current estimate. Starting with a given initial estimate $m(0)$, at each iteration t, one proves that the likelihood $p(S|m(t))$ increases. Following Shepp & Vardi (1982), by derivating expression (6), we find the classical update formula for a single voxel m_r:

$$m_r(t+1) = m_r(t)\,\frac{1}{\sum_{k,j} \mathcal{H}_{r,j}^k} \sum_{k,j} \mathcal{H}_{r,j}^k \frac{S_j^k}{\sum_l \mathcal{H}_{l,j}^k m_l(t)}\,.$$

In Lucy (1974), the term $1/\sum_{k,j} \mathcal{H}_{r,j}^k$ is not present, and in Shepp & Vardi (1982) the term $H_{r,j}^k$ does not depend on k. In this formula, the update term that is applied to $m_r(t)$, can be interpreted as follows. Since $\sum_l \mathcal{H}_{l,j}^k m_l(t)$ is the current estimation of the expectation $\mathrm{E}(S_j^k)$, the update is driven by the ratio between S_j^k and this estimated expectation. Furthermore, on this formula we see the interpolation effect of this method. When r corresponds to a point between two F^k or to a point in the black hole, the update term sums data S_j^k over a region whose range is defined by the PSF support.

By denoting ./ the element-wise division and defining γ so that $\gamma_i = \sum_{k,j} \mathcal{H}_{i,j}^k$, we can use matrix notation for the update step:

$$m(t+1) = (m(t)./\gamma) \sum_k (\mathcal{H}^k)^\top \left(S^k./(\mathcal{H}^k m(t))\right)\,. \tag{7}$$

Such a writing helps to implement the algorithm using the FFT, and thus allows acceptable computational times.

Experimental results

Acquisition

The experiments shown below were performed on a sequence of real micro-rotated images. Cultured SW13/20 living cells (human tumour cell lines) tagged nuclear targeted green fluorescent protein (lamin-A-GFP, a kind gift of Christopher Hutchinson) were suspended in a DFC-3 chip (Evotec Technologies/Perkin Elmer group, Germany) controlled by a Cytocon400TM's 4-phase high frequency generator (Evotec Technologies). Individual cells were rotated around the x–y axis and imaged using an Andor Revolution XD spinning disk

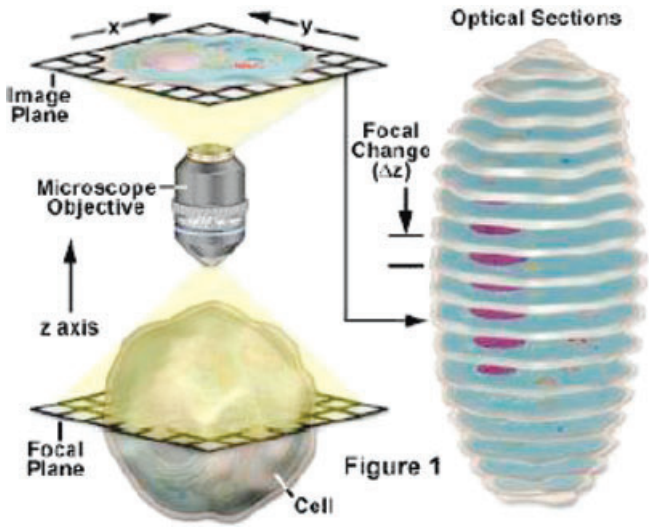

Fig. 4. z-stack protocol.

confocal system equipped with an EM-CCD DV885 camera (Andor Technology, Belfast Northern Ireland) mounted on an inverted microscope (Axiovert 200M, Carl Zeiss, Germany). The microscope is equipped with a 63× water immersion objective with a numerical aperture (NA) 1.2. Fluorescence acquisition used laser light excitation 488 nm and emission band-pass filter 500–550 nm.

Furthermore, our spinning disk confocal microscope is equipped with an objective piezo-drive. So, in addition to the micro-rotation sequence, a so-called axial "through-stack" image series (or "z-stack") is recorded from the target samples immobilized in suspension, (see Fig. 4). The piezo step in through-stack axial imaging was 100 nm and xy resolution was 127 nm. More details about z-stack acquisition can be found in (Renaud *et al.*, 2008).

The choice of the appropriated PSF is crucial. Several approaches exist: computing the PSF from a theoretical physical model (der Voort & Strasters, 1994), measuring the PSF directly from the microscope, or estimating the PSF from the images (Chalmond, 1991). We have experimented with the two first approaches. To measure the point spread function, 3D image stacks are acquired from subresolution beads (0.17 μm, Molecular Probes) suspended in the same medium used for live-cell imaging, and using the same microscope configuration. The calculated axial resolution is 591 nm (microscope resolution calculator[1]) and the axial sampling interval is 100 nm. Image data from five to eight independent measurements were averaged and the PSF is calculated using Huygens Pro software (Scientific Volume Imaging, the Netherlands). The 3D image Ψ is given from a z-stack of this bead according to the protocol used for acquiring

[1] http: //www.pfid.org/html/objcalc/?en

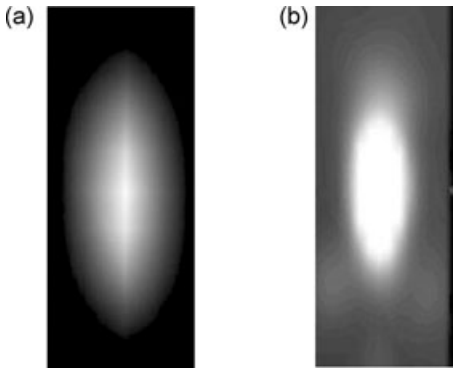

Fig. 5. Theoretical PSF and measured PSF.

cell images. The measured PSF Ψ and the theoretical PSF are depicted in Fig. 5.

Deconvolution-interpolation results

The experiments aim to test the quality of the results. The first round of experiments compares the original data (i.e., micro-rotated images obtained by the microscope) with micro-rotated images in the reconstructed volume after deconvolution, taken at the same position. Results are shown in Fig. 6. The deconvolution process reveals details of the cell, like swellings or folds of the cell membrane. In Fig. 7, we also compare our results with the 3D reconstruction obtained by interpolation as described in section 'Interpolation without deconvolution'. The advantage of our deconvolution approach is twofold. First, more details are visible, which is the expected result of the deconvolution. Second, as others inversion methods, our approach has an interpolation effect that is able to deal with the incomplete coverage, contrary to the simple interpolation method. On some views of the left column of Fig. 7 (see also Fig. 8(b)), a black hole is visible. Such an artifact occurs when the focal plane turns around an axis that is not included in it, and in this case a part of the 3D space—which has the shape of a cone—is not covered by the moving plane. Since no data are captured in this area, the simple interpolation approach replaces it by a black hole. On the contrary, the deconvolution approach uses the PSF to propagate information and find an estimate of the voxel values at those locations (and thus fill the black hole). In our experiment, the PSF has a size of 7 × 7 pixels in the xy-plane whereas the maximal hole size is not greater than 5 (the angle between the rotation axis and the focal plane is around 5 to 6°). Therefore, during the deconvolution process, most often one slice has interaction with its two neighbour slices what is a favourable case for the success of the deconvolution.

A second round of experiments compares these two first cell reconstructions with the cell obtained from a z-stack (see Figs. 8–10). In the absence of ground true, z-stack data are the main reference. Images show distribution of a nucleoskeletal

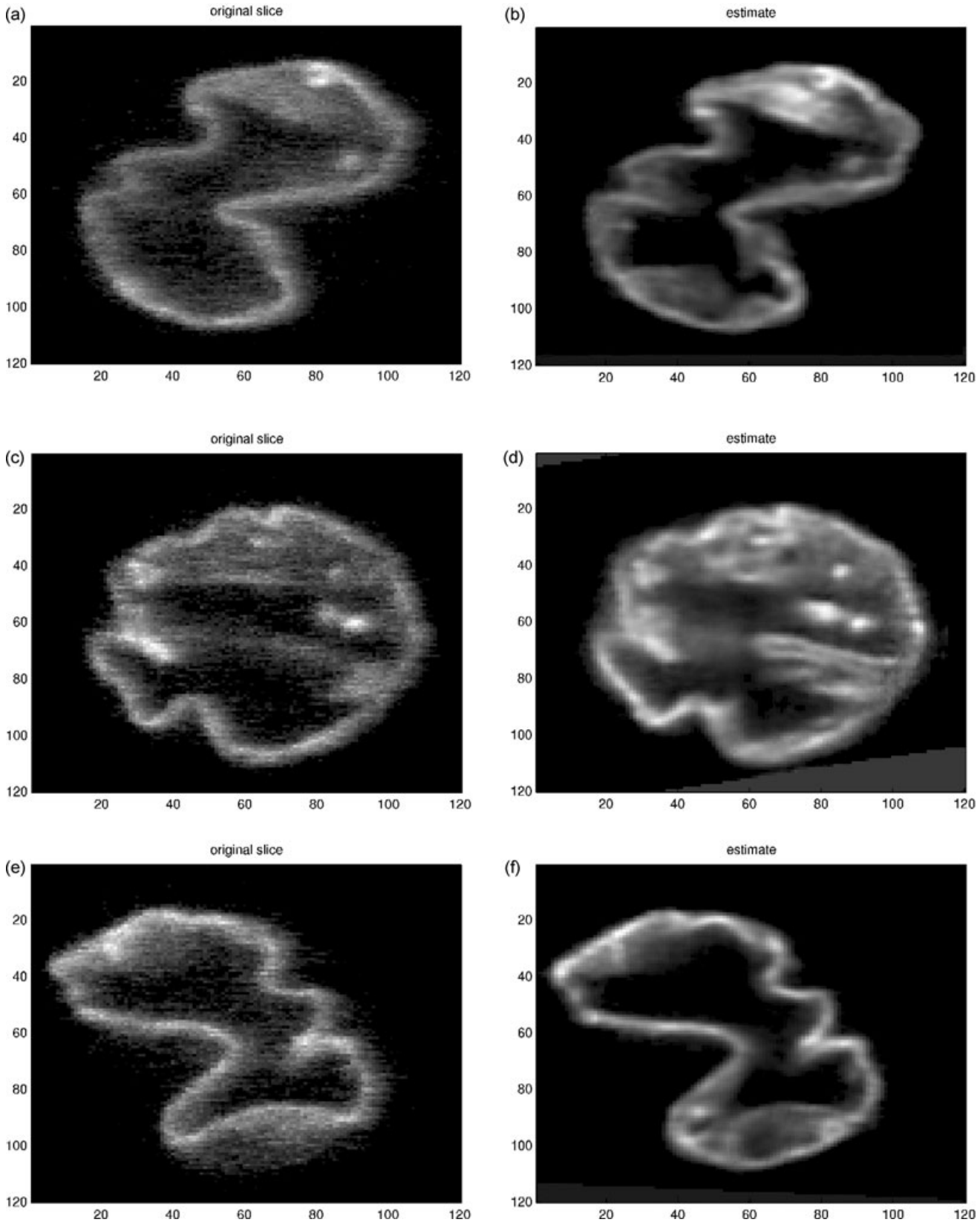

Fig. 6. Comparison of original micro-rotated images (first column) with the corresponding micro-rotated images in the deconvolved volume (second column). The xy microscope resolution is 127 nm. The difference of view between two successive rows corresponds to a quarter-turn of the focal plane.

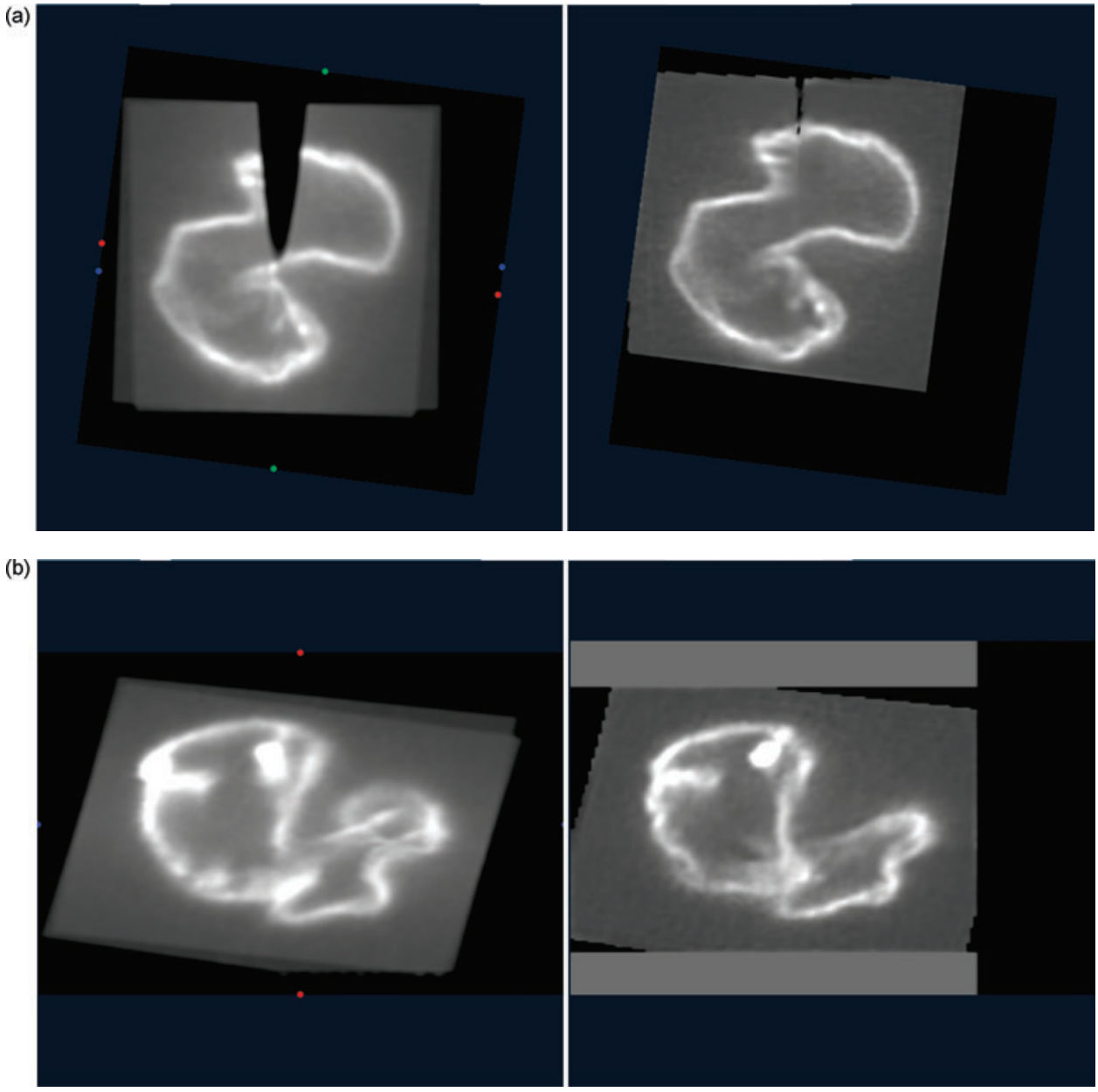

Fig. 7. Comparison of two reconstruction methods (The difference of view between two successive rows corresponds to a quarter-turn of the cross-section. These orientations are those depicted in Fig. 8). First column: micro-rotated images are taken from the volume obtained by interpolation with Gaussian kernels. Second column: micro-rotated images are taken from the volume obtained by the EM deconvolution process.

intermediate filament protein (lamin) distributed in the periphery of the nuclear envelope. Micro-rotation volume reconstruction shows 3D-image enhancement. Many details are revealed using this imaging modality, particularly the nuclear envelope invagination through the nucleus and others that are not present on the z-stack volume (see for example the element marked by a square). Figure 9 illustrates the gain in isotropy for the micro-rotation imaging in comparison with the z-stack imaging. In particular, some blob-shape elements marked by an arrow are much more elongated in the z-stack volume than in the micro-rotation one. It could help quantifying the gain in resolution. Unfortunately, matching these elements between two reconstructed volumes is a hard task that cannot be done simply because matching must be done in 3D. This problem is under study.

A third round of experiment is based on simulation. The microscopic simulation workbench consists of tools to build synthetic objects that realistically represent biological objects

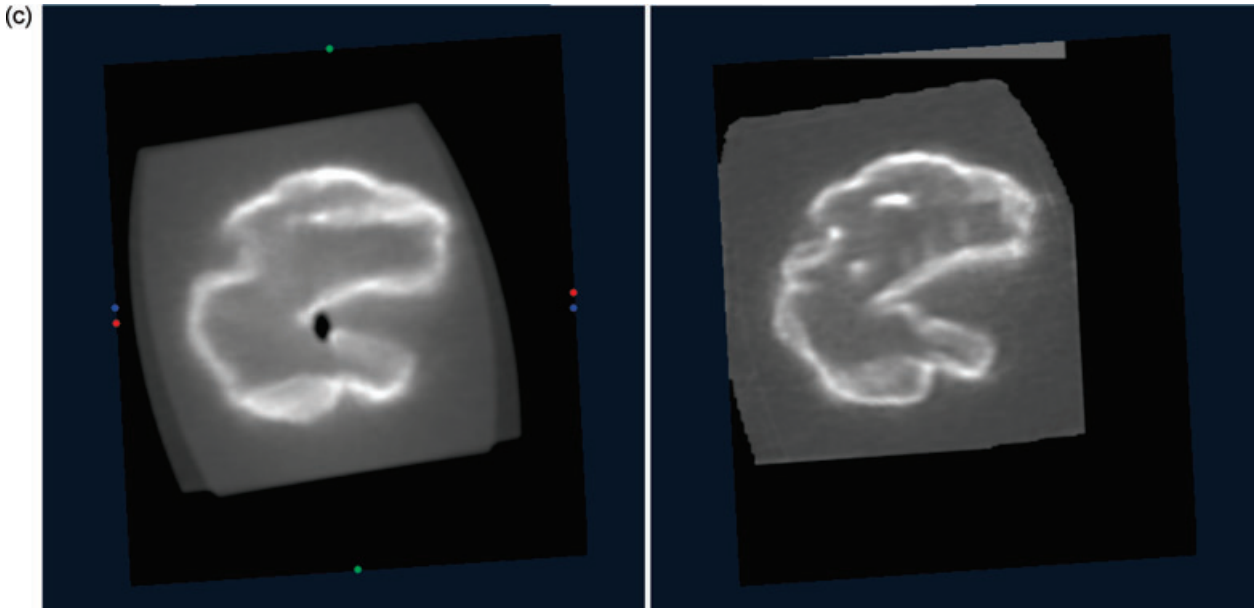

Fig. 7c. Continued.

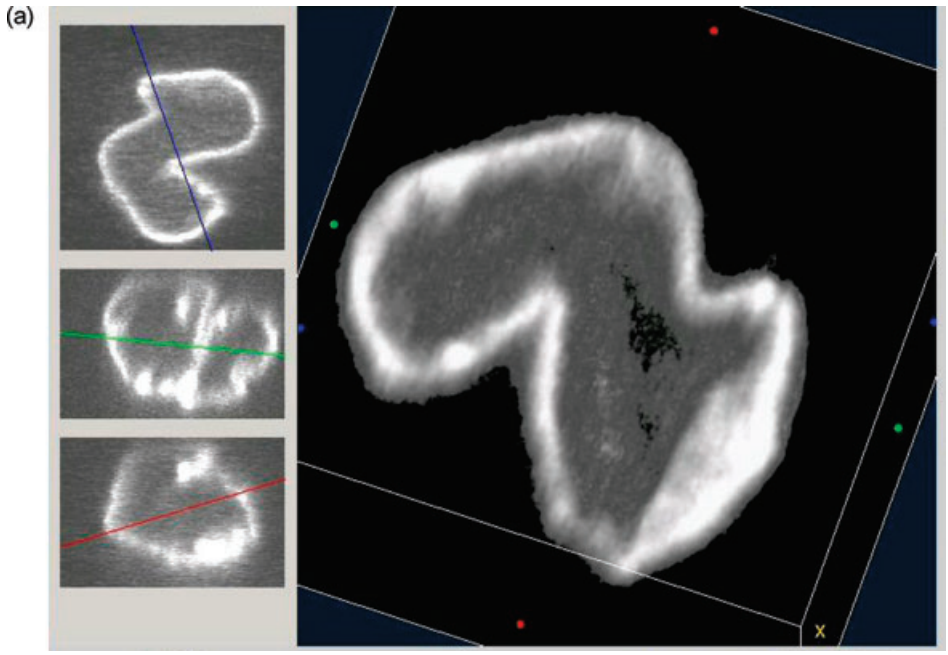

Fig. 8. Volume rendering with ImageJ software (The lines on the slices depicted on the right side of the volume rendering, give its orientation). (a) z-stack reconstruction, (b) MR reconstruction without deconvolution (the artefact due to the black hole is clearly apparent), (c) the same with deconvolution (the black hole artefact has been removed).

and simulate the microscopic image formation of multiple orientations of these. The simulator is a means to test some aspects of the reconstruction methods by simulating different kind of movement and degradation. Here we use this simulator to study the impact of position errors on the reconstruction results. The errors are the result of a trembling: every plane F^k is translated along the rotation axis according to a Gaussian law $\mathcal{N}(0, \tau^2)$. Twelve values of τ have been chosen: $\tau_q = q/2, q = 1, \ldots, 12$, and for every τ_q, n_q simulations and reconstructions have been performed. For every simulated

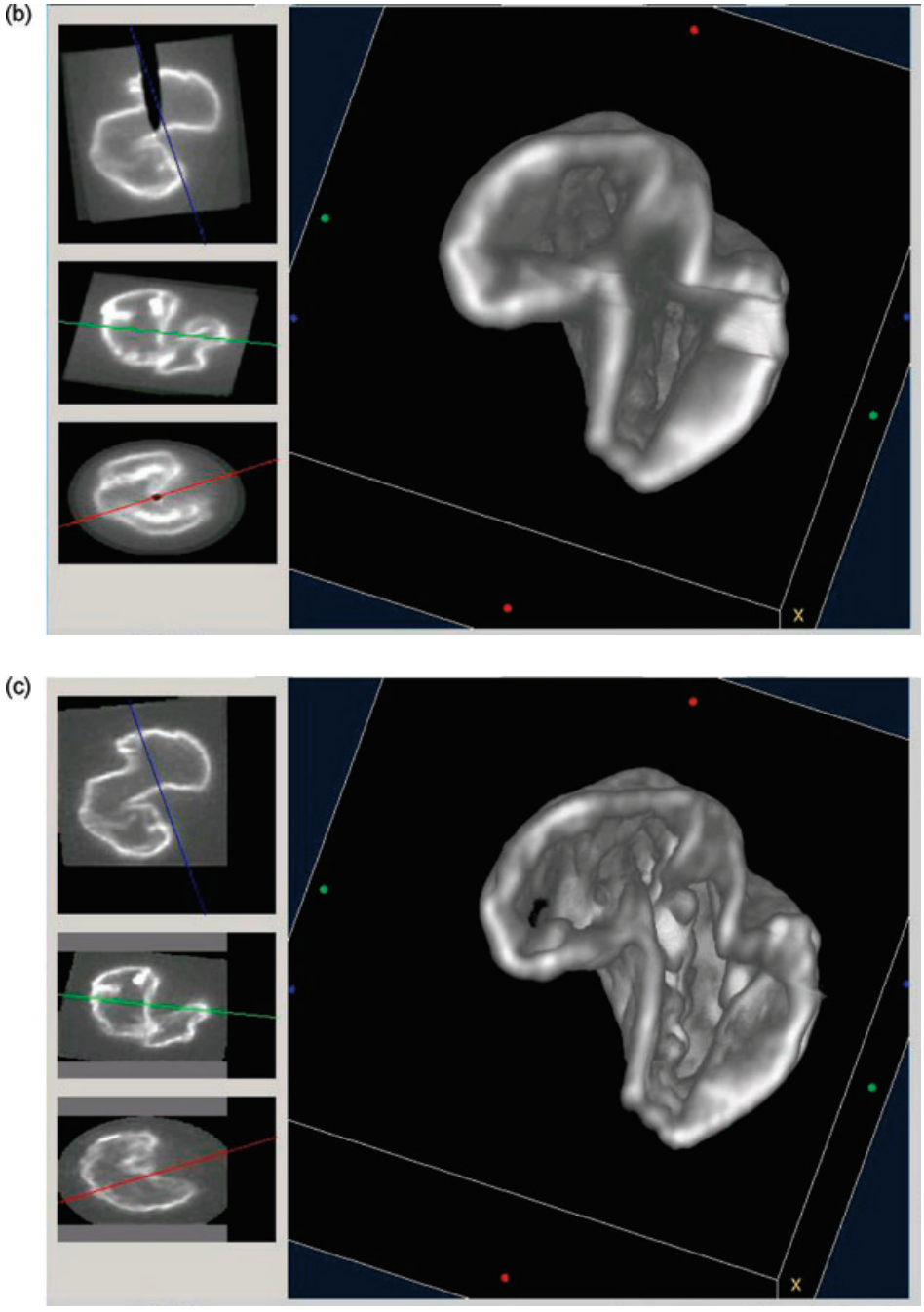

Fig. 8. Continued.

data set, the quality of the reconstruction is measured by the Peak-Signal-to-Noise-Ratio:

$$PSNR_l(\tau_q) = 20 \log_{10} \left(\frac{\max m}{\|m - \hat{m}_l^{(q)}\|} \right), \quad l = 1, \ldots, n_q,$$

where m denoted the true volume and $\hat{m}_l^{(q)}$ is the reconstructed volume. Figure 11 shows the mean PSNR curve $\overline{PSNR}(\tau_q)$, $q = 1, \ldots, 12$ and Figs. 12 and 13 show the reconstructed volume after deconvolution for $\tau = 2.5$, in comparison to the true volume m.

Let us briefly speak about some others experiments we have done. Deconvolution is typically an inverse problem. In such a context, it is well known that introducing prior knowledge on the unknown parameters m is needed to stabilize and improve the solution (cf. Chalmond, 2003; Chan & Shen, 2005, among

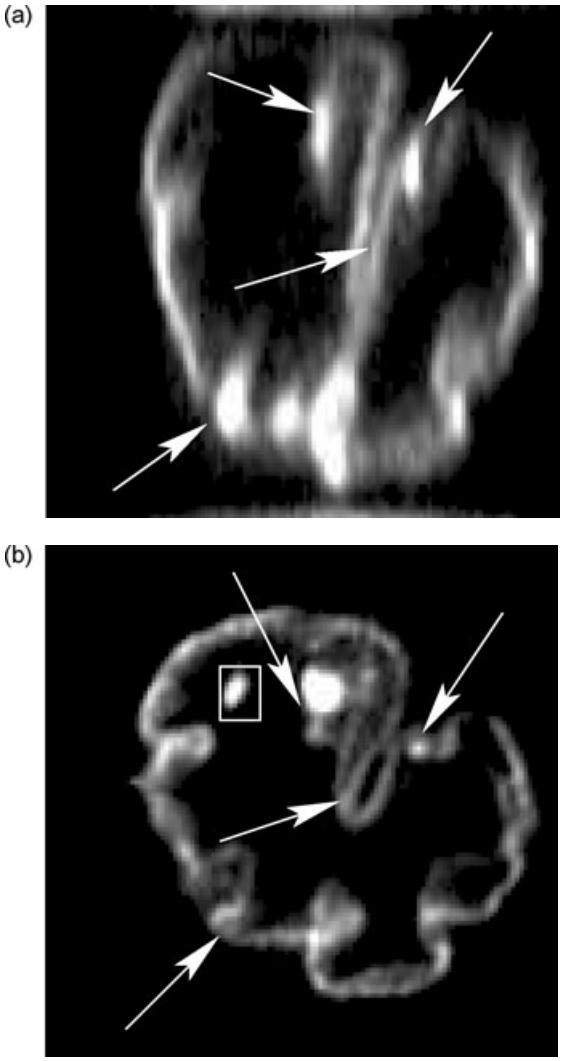

Fig. 9. xz slice from the reconstructed volume (optical axis is vertical): (a) z-stack volume, (b) micro-rotation volume.

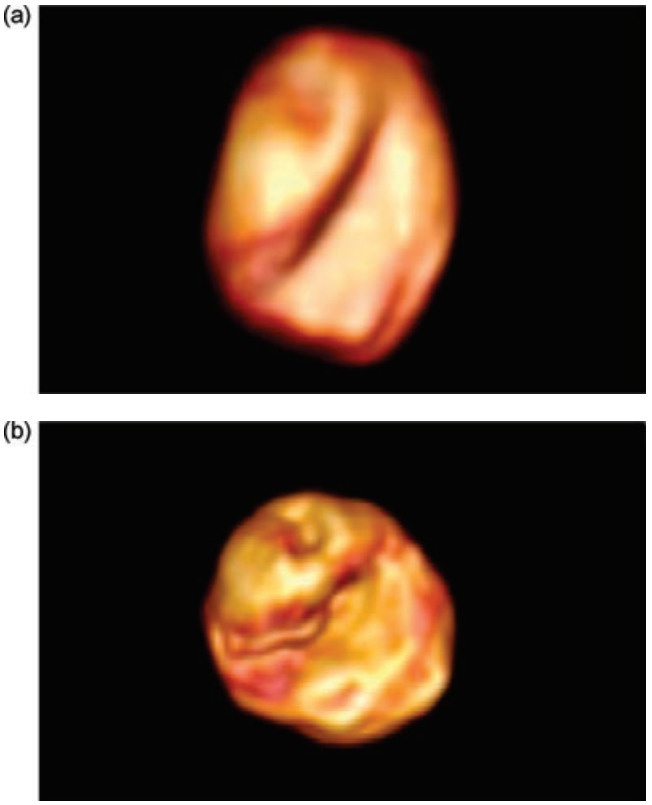

Fig. 10. Volume rendering (optical axis is vertical): (a) z-stack volume, (b) micro-rotation volume.

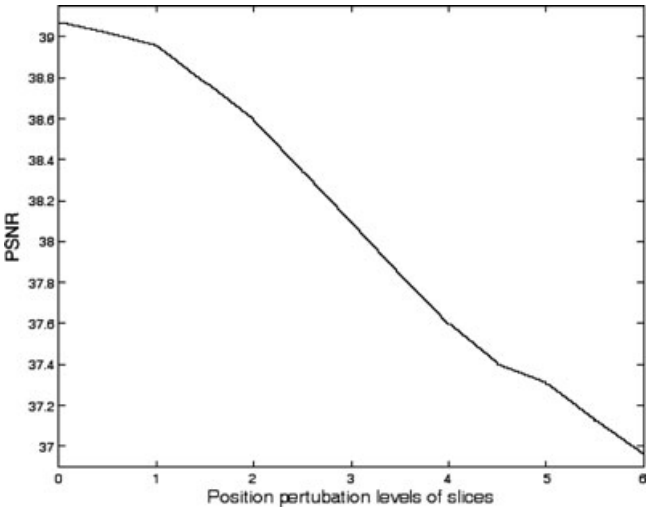

Fig. 11. PSNR curve with regard to the standard deviation of the position errors.

many others). Naturally, we have also searched to integrate a regularization component in our deconvolution process. As in section 'Interpolation without deconvolution', it consists to replace the likelihood $p(x|m)$ in (6) by the penalized likelihood $p(x|m)\ p(m)$ where the distribution $p(m)$ translates our prior knowledge. From Geman & McLure (1985), many prior distributions have been studied (Chalmond, 1989; Hebert & Lehay, 1989; Green, 1990; Lange, 1990; Charbonnier *et al.*, 1997; De Pierro & Yamagishi, 2001; Gravier & Yang, 2005; Mair & Zahnen, 2006). We have tested several regularization terms and in particularly the Total Variation term as used for confocal image deconvolution in Dey *et al.*, (2006). The role of this prior is to recover a smooth solution with sharp edges, but in the light of the experimental results, we found the counterintuitive result whereby regularization as total variation does not yield significant improvement over the micro-rotation deconvolution for real data.

Conclusion

Deconvolution of micro-rotated image series, as presented here, yields a striking improvement in data quality including a strong reduction in two-dimensional out-of-focus blur. This is due to efficient 3D light reconstruction whereby

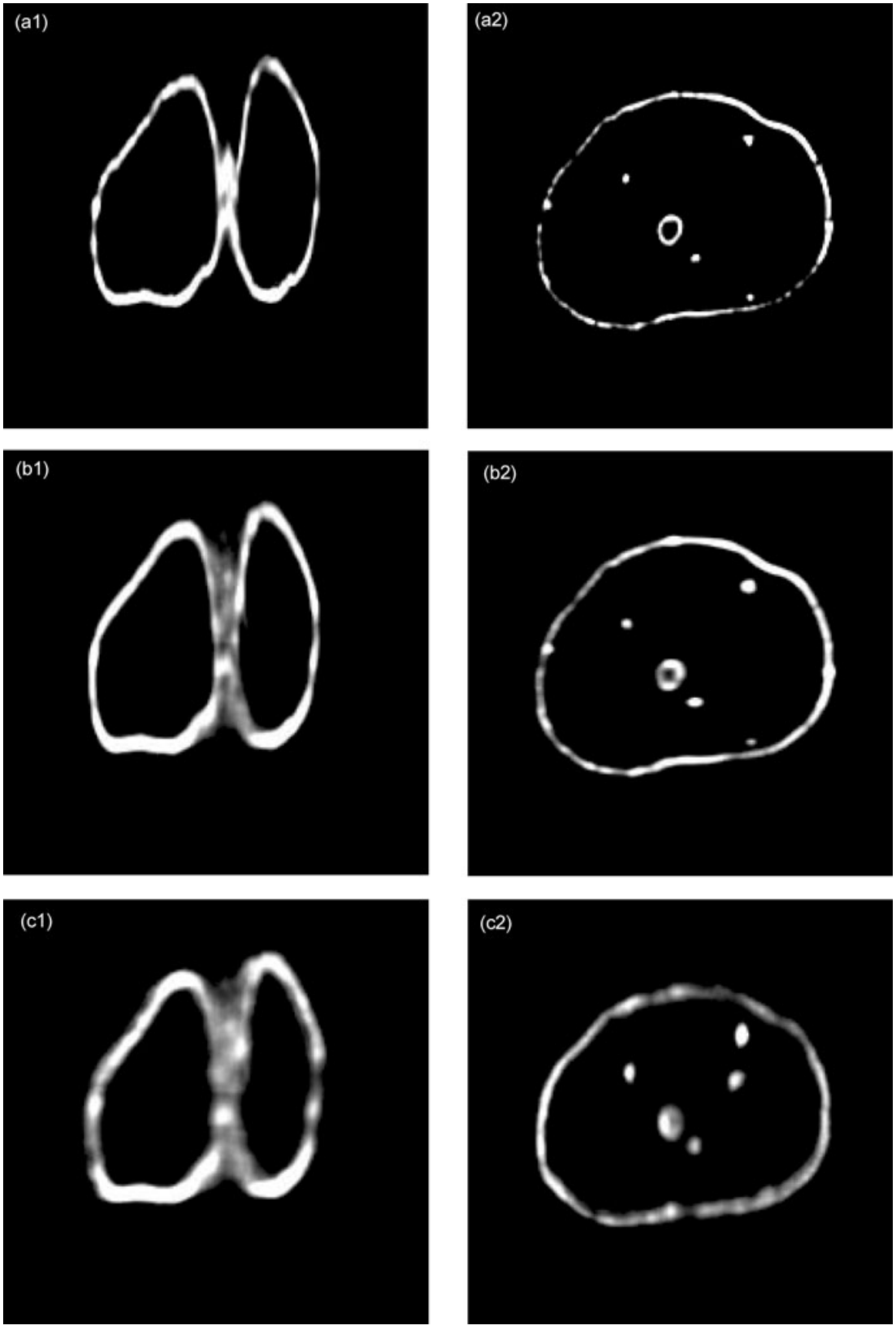

Fig. 12. Sagittal and transaxial views for simulated data. (a) True volume. (b) Reconstructed volume without position error. (c) Reconstructed volume with position errors ($\tau = 2.5$).

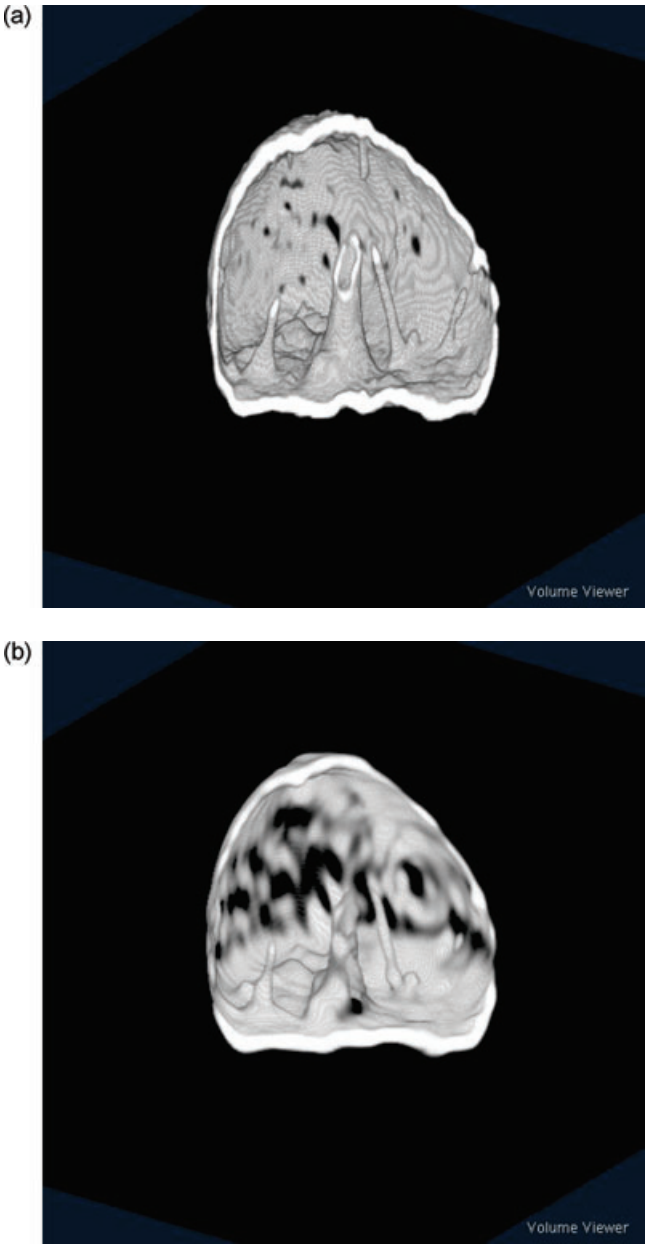

Fig. 13. Volume rendering for simulated data. (a) True volume. (b) Reconstructed volume without position error. (c) Reconstructed volume with position errors ($\tau = 2.5$).

the PSF geometry and pitch orientation guides accurate 3D reassignment of out-of-focus light emanating from fluorescent features of interest. A most unexpected observation, and apparently peculiar to this novel imaging modality is the remarkable efficacy of light reconstruction by deconvolution. We show that in the case where information is lost in micro-rotation feature reconstruction due mainly to incomplete sampling near the rotation axis (i.e., the black-hole artefact) that such information is fully recovered by the

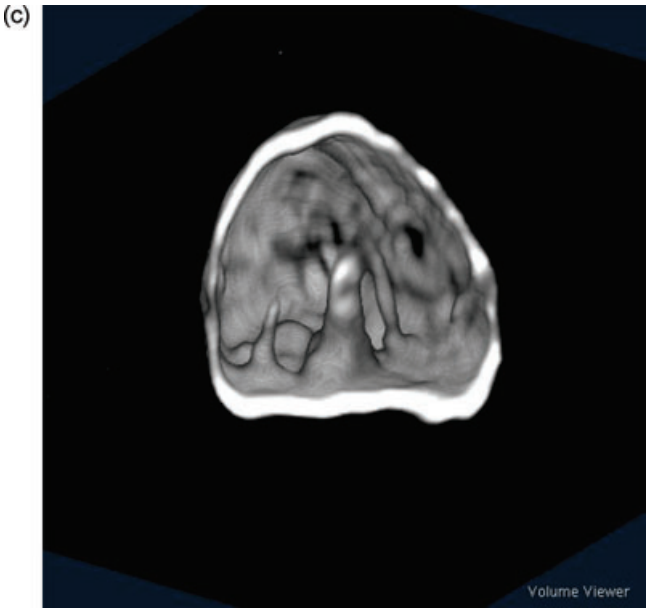

Fig. 13. Continued.

deconvolution process. This interpolation effect presumably arises due to the rotating PSF, and to our knowledge has yet to be characterized. Our results suggest thatdeconvolution of micro-rotation image series open some exciting new avenues for further analyses, ultimately laying the way towards establishing an enhanced resolution 3D light microscopy.

Acknowledgements

This research has been supported by the French Ministry of Research (grant ANR Emergence 2007) and by the European Commission (FP6 NEST 2005 programme) in consortium AUTOMATION (http://www.pfid.org/AUTOMATION/home/) and by the "Conseil de la Région Ile-de-France" (programme SESAME 2007). SW13/20 cells were kindly provided by Christopher Hutchinson (School of Biological and Biomedical Sciences, Durham University, UK). The figures 1 and 2 use figures adapted from originals supplied by Evotec Technology. The figure 4 is lifted directly from the site 'molecular expressions' authored by M. W. Davidson. We also thanks Christophe Machu and Anne Danckaert from the PFID for their technical support.

References

Chalmond, B. (1989) An iterative Gibbsian technique for reconstruction of m-ary images. *Pattern Recognit.* **22**, 747–761.

Chalmond, B. (1991) PSF estimation for image deblurring. *CVGIP: Graphic. Models and Image Process.* **53**, 364–372.

Chalmond, B. (2003) *Modeling and Inverse Problems in Image Analysis*. Springer-Verlag, New York.

Chan, T. & Shen, J. (2005) *Image Processing and Analysis*. SIAM, Philadelphia.

Charbonnier, P., Blanc-Feraud, L., Aubert, G. & Barlaud, M. (1997) Deterministic edge-preserving regularization in computed imaging. *IEEE Trans. Image Process.* **6**, 298–311.

De Pierro, A.R. & Yamagishi, M.E.B. (2001) Fast EM-like methods for maximum "a posteriori" estimates in emission tomography. *IEEE Trans. Med. Imag.* **20**, 280–288.

Dempster, A., Laird, N. & Rubin, D. (1977) Maximum likelihood from incomplete data via the EM algorithm. *J. R. Stat. Soc. B* **39**, 1–38.

Dey, N., Blanc-Fèraud, L., Zimmer, C., Kam, Z., Roux, P., Olivo-Marin, J. & Zerubia, J. (2006) Richardson-Lucy algorithm with total variation regularization for 3-D confocal microscope deconvolution. *Microsc. Res. Tech.* **69**, 260–266.

Geman, S. & McLure, D. (1985) Bayesian image analysis: an application to single photon emission tomography. *In Proceedings of the Statistical Computing Section, American Statistical Association*, 12–18.

Gravier, E.J. & Yang, Y. (2005) Motion-compensated reconstruction of tomographic image sequences. *IEEE Trans. Nucl. Sci.* **52**, 51–56.

Green, P. (1990) On use of EM algorithm for penalized likelihood estimation. *J. R. Stat. Soc. B* **52**, 443–452.

Hebert, T. & Lehay, R. (1989) A generalized EM algorithm for 3-D Bayesian reconstruction from Poisson data using Gibbs priors. *IEEE Trans. Med. Imag.* **8**, 194–202.

Hudson, H. & Larkin, R. (1994) Accelerated image reconstruction using ordered subsets of projection data. *IEEE Trans. Med. Imag.* **13**, 601–609.

Laksameethanasan, D., Brandt, S. & Engelhardt, P. (2006) A three-dimensional Bayesian reconstruction method with the point spread function for micro-rotation sequences in wide-field microscopy. In *IEEE International Symposium on Biomedical Imaging (ISBI 2006)*, Arlington, USA.

Laksameethanasan, D., Brandt, S., Engelhardt, P., Renaud, O. & Shorte, S. (2008) A Bayesian reconstruction method for micro-rotation imaging in light microscopy. *Microsc. Res. Tech.* **71**, 158–167.

Lange, K. (1990) Convergence of EM image reconstruction algorithms with Gibbs smoothing. *IEEE Trans. Med. Imag.* **9**, 439–446.

Lizundia, R., Sengmanivong, L., Guergnon, J., Muller, T., Schnelle, T., Langsley, G. & Shorte, S. (2005) Use of micro-rotation imaging to study JNK-mediated cell survival in theileria parva-infected b-lymphocytes. *Parasitology* **130**, 629–635.

Lucy, L. (1974) An iterative technique for the rectification of observed distributions. *Astron. J.* **79**, 745–754.

Mair, B.A. & Zahnen, J. (2006) A generalization of Green's one-step-late algorithm for penalized ML reconstruction of pet images. In *IEEE Nucl. Sci. Symp. Conf. Record*, M11–361:2775–2778.

Renaud, O., Vina, J., Yu, Y., Machu, C., Trouvé, A., Van der Voort, H., Chalmond, B. & Shorte, S. (2008) High-resolution imaging of living cells in flow suspension using axial-tomography: 3-D imaging flow cytometry. *Biotechnol. J.* **3**, 53–62.

Richardson, W. (1972) Bayesian-based iterative method of image restoration. *J. Opt. Soc. Am.* **62**, 55–59.

Schnelle, T., Hagedorn, R., Fuhr, G., Fielder, S. & Muller, T. (1993) Three-dimensional electric field traps for manipulation of cells—calculation and experimental verification. *Biochim. Biophys. Acta* **1157**, 127–140.

Shepp, L.A. & Vardi, Y. (1982) Maximum likelihood reconstruction in positron emission tomography. *IEEE Trans. Med. Imag.* **1**, 113–122.

Shorte, S., Muller, T. & Schnelle, T. (2003) *Method and device for 3 dimensional imaging of suspended micro-objects providing high-resolution microscopy*. Patent International Application No.PCT/EP2003/011818.

der Voort, H.V. & Strasters, K. (1994) Restoration of confocal images for quantitative image analysis. *J. Microsc.* **178**, 165–181.

Wahba, G. (1999) *Advances in Kernel Methods* chap. Support vector machines, reproducing kernel Hilbert spaces and the randomized GACV, 69–88. MIT Press.

Yu, Y., Trouvé, A. & Chalmond, B. (2007) A Bayesian 3-D volume reconstruction for confocal micro-rotation cell imaging. In *Medical Image Computing and Computer-Assisted Intervention—Proc. of MICCAI 2007* edited byN. Ayache, S. Ourselin & A. Maeder, 685–692.

Yu, Y., Trouvé, A., Wang, J. & Chalmond, B. (2008) An integrated statistical approach for volume reconstruction from unregistered sequential slices. *Inverse Problems* **24**, 58–74.